MICROROBOTS

Magnetic torque–driven living microrobots for increased tumor infiltration

T. Gwisai[1], N. Mirkhani[1], M. G. Christiansen[1], T. T. Nguyen[1]†, V. Ling[2], S. Schuerle[1]*

Biohybrid bacteria–based microrobots are increasingly recognized as promising externally controllable vehicles for targeted cancer therapy. Magnetic fields in particular have been used as a safe means to transfer energy and direct their motion. Thus far, the magnetic control strategies used in this context rely on poorly scalable magnetic field gradients, require active position feedback, or are ill-suited to diffuse distributions within the body. Here, we present a magnetic torque–driven control scheme for enhanced transport through biological barriers that complements the innate taxis toward tumor cores exhibited by a range of bacteria, shown for *Magnetospirillum magneticum* as a magnetically responsive model organism. This hybrid control strategy is readily scalable, independent of position feedback, and applicable to bacterial microrobots dispersed by the circulatory system. We observed a fourfold increase in translocation of magnetically responsive bacteria across a model of the vascular endothelium and found that the primary mechanism driving increased transport is torque-driven surface exploration at the cell interface. Using spheroids as a three-dimensional tumor model, fluorescently labeled bacteria colonized their core regions with up to 21-fold higher signal in samples exposed to rotating magnetic fields. In addition to enhanced transport, we demonstrated that our control scheme offers further advantages, including the possibility for closed-loop optimization based on inductive detection, as well as spatially selective actuation to reduce off-target effects. Last, after systemic intravenous injection in mice, we showed significantly increased bacterial tumor accumulation, supporting the feasibility of deploying this control scheme clinically for magnetically responsive biohybrid microrobots.

INTRODUCTION

Biohybrid microrobots that combine cellular and synthetic components hold promise for improved cancer treatment because of their ability to propel themselves, autonomously respond to biochemical cues, and carry therapeutic payloads (*1*). Microrobots based on bacteria are particularly appealing because of their immune modulating capabilities as well as the innate tumor homing and preferential colonization exhibited by certain bacterial strains (*2*–*5*). Outside the robotics community, the direct use of bacteria in cancer treatment has been investigated for more than a century, and a wide range of genetically engineered and attenuated strains have been tested in various animal models (*6*). Moreover, strains of *Salmonella*, *Mycobacterium*, and *Clostridium* have progressed to human clinical trials for bacteria-based cancer therapy (*7*–*10*). Nevertheless, translation of this approach has been hindered by incomplete clinical responses, due, in part, to insufficient tumor colonization (*11*). Developing control strategies to enhance and accelerate accumulation of bacteria within tumors is essential to limit immune clearance, facilitate robust colonization, and lower the required dose of bacteria, thus increasing therapeutic efficacy and safety.

The use of biohybrid microrobots seeks to address this challenge by enabling wireless control through engineered responses to external stimuli, including chemical gradients, light, electric fields, and magnetic fields (*12*–*16*). Of these, magnetic fields are especially promising for medical use because of their minimally invasive deep tissue penetration and well-established clinical safety (*17*). Magnetically responsive bacteria include strains rendered magnetic through conjugation with magnetic materials (*18*–*20*) and magnetotactic bacteria (MTB), which are innately magnetic. In their native aquatic habitats, MTB typically biomineralize stably magnetized anisotropic chains of magnetite nanocrystals and use magnetically assisted aerotaxis to migrate to regions of low oxygen concentration. In vivo, strains of MTB carrying payloads have been shown to preferentially proliferate in deoxygenated regions of tumors after peritumoral injection in the presence of a directional magnetic field (DMF) or a magnetic field gradient (*21*, *22*).

Although magnetic bacteria–based microrobots are promising drug delivery agents, their potential for clinical translation has been curbed so far by limitations associated with the magnetic control strategies applied to them. Drawing them toward target sites with static field gradients has fundamental shortcomings, especially in the context of deep tumors, because magnetic field gradients rapidly diminish with increasing distance from their source (*23*, *24*). Using DMF inherently relies on positional information about the microrobots with respect to the target site. Hence, this control strategy is unsuitable for systemic injection because this would result in dispersed distributions of the microrobots within the body. Instead, peritumoral administration is required for DMF control, which can only be applied to easily accessible tumors.

In this work, we established a hybrid control strategy that harnesses magnetic torque–driven motion followed by autonomous taxis–based navigation to enhance the infiltration of *Magnetospirillum magneticum* strain AMB-1 as a magnetically responsive model organism and a carrier for covalently coupled liposomes (MTB-LP) (Fig. 1). Unlike some forms of magnetic stimulus, uniform rotating magnetic fields (RMF) can be generated at clinically relevant scales to control systemically dispersed microrobots, independent of visual feedback. In previous work, we demonstrated the ability of

[1]Department of Health Sciences and Technology, Institute for Translational Medicine, ETH Zürich, 8092 Zürich, Switzerland. [2]Takeda Pharmaceuticals, 40 Landsdowne St., Cambridge, MA 02139, USA.
*Corresponding author. Email: simone.schuerle@hest.ethz.ch
†Present address: Roche Pharma Research and Early Development, Wagistrasse 10, 8952 Schlieren, Switzerland.

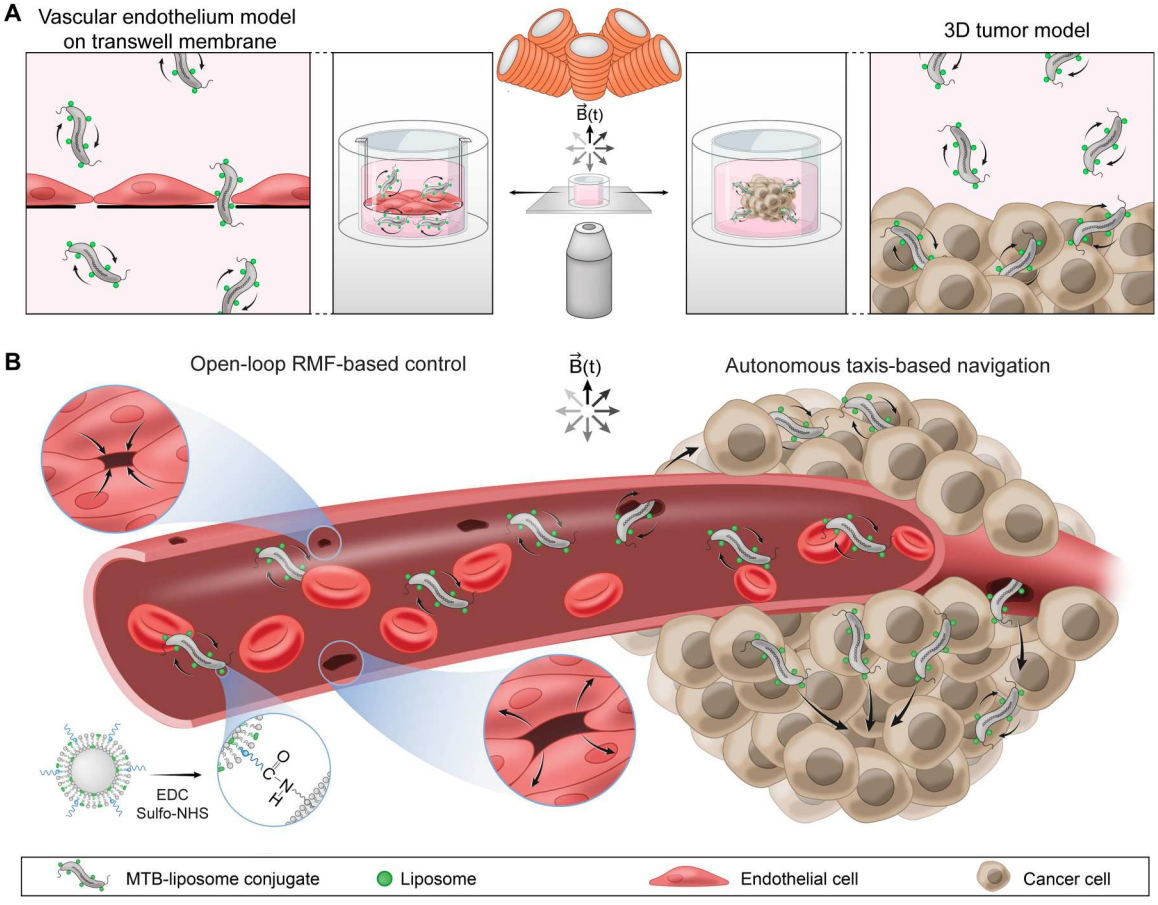

Fig. 1. Conceptual overview of hybrid control scheme for magnetically enhanced MTB-liposome conjugate transport. (**A**) Integrated magnetic manipulation and imaging setup used in experiments to analyze the transport of MTB-liposome conjugates in a vascular endothelium model and a 3D tumor model. (**B**) Samples are placed between the objective lens and electromagnetic coils, which generate a uniform RMF, and MTB-liposome conjugates rotate individually in response to the applied field. (**B**)Schematic illustrating magnetically controlled transport of MTB-liposome conjugates through a blood vessel with dynamic cell gap openings and into a tumor.

MTB exposed to RMF to effectively generate volumetric flows for local fluid convection to enhance the transport of nonmagnetic nanoparticles across collagen matrices in microfluidic models (*25*, *26*). Here, instead, we showed the potential of RMF for remote, open-loop control of MTB as magnetically responsive model organisms by significantly enhancing their translocation across tissue barriers and colonization of target tissues. Using the Caco-2 Transwell system, we established that RMF increases MTB translocation across this barrier compared with DMF or the absence of magnetic actuation. We also demonstrated other intrinsic advantages of control by RMF. This includes its suitability for simultaneous actuation and inductive detection, which could be exploited for real-time monitoring and closed-loop operational optimization. We additionally demonstrated the ability for spatially selective RMF actuation via the superposition of magnetostatic gating fields with the potential to reduce off-target effects. We then assessed MTB-LP infiltration in the presence of RMF using model tissue barriers. By studying extravasation with computational models and in vitro experimentation, we found that the main mechanism driving the enhancement of translocation is increased surface exploration resulting from torque-driven translational motion at the cell interface. Next, we analyzed the spatiotemporal characteristics of magnetically driven MTB-LP infiltration and found enhanced colonization in a three-dimensional (3D) tumor model.

Last, we demonstrated enhanced MTB tumor accumulation under RMF in vivo while also using more clinically relevant systemic intravenous administration. We conclude that the MTB-LP platform combined with an RMF actuation scheme is a versatile biohybrid system that could improve targeting and colonization of therapeutic bacteria and bacteria-based microrobots in tumors. This work also lays the foundation for effective torque-based transport of other bacterial microrobots imparted with magnetic responsiveness through genetic engineering or magnetically anisotropic surface functionalization.

RESULTS

RMFs enhance bacterial translocation and offer unique control advantages

A range of strategies have previously been used to manipulate MTB as living microrobots using external magnetic fields (Fig. 2A). In the presence of DMF, the motion of the bacteria is dependent on the propulsive force ($\mathbf{F}_P$) generated by their flagella and the fluidic drag force ($\mathbf{F}_D$), which are equal and opposite when traveling at

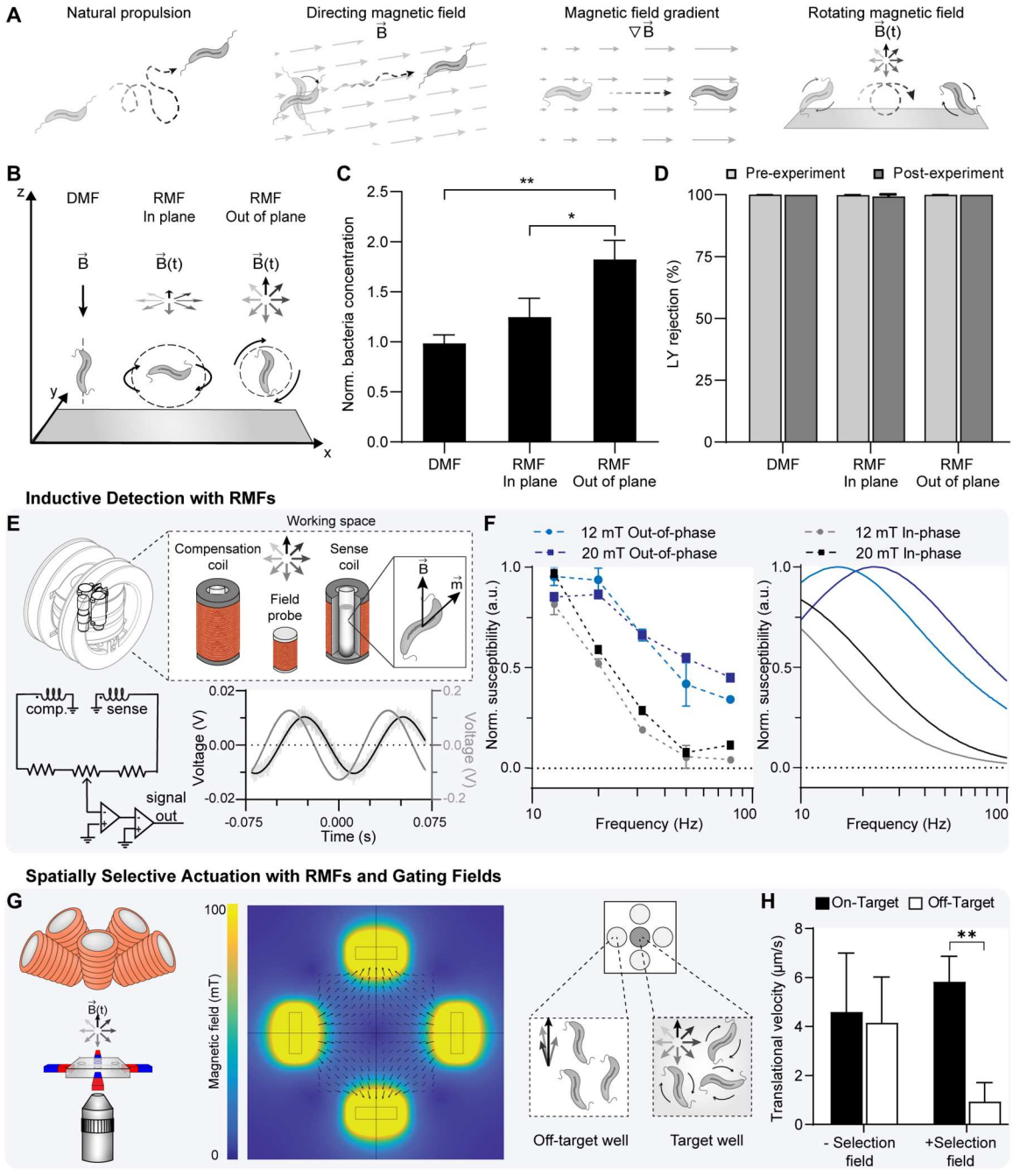

Fig. 2. RMF enhance translocation and enable inductive detection and spatially selective control of MTB. (**A**) Schematic illustrating various magnetic actuation strategies used to manipulate MTB. (**B**) Schematic depicting the reference coordinate system used in all actuation experiments and orientation of the bidirectional MTB strain (AMB-1) after exposure to static directional magnetic fields (DMF) and in-plane and out-of-plane RMFs. (**C**) Comparison of normalized basolateral bacteria concentrations after 1 hour of exposure to DMF, either in-plane rotation or out-of -plane rotation, both at 14 Hz. In these experiments only, a magnetic force generated by spatial variation of the magnitude of the RMF or DMF (1 T/m) was applied along −*z*. Bacteria concentration was normalized to respective unactuated controls ($n = 3$; means ± SD; $^{*}P < 0.05$ and $^{**}P < 0.01$, ANOVA). (**D**) Pre- and post-experimental LY rejection values for DMF and in plane and out of plane RMF ($n = 3$; means ± SD). (**E**) Cancellation and amplification scheme for RMF magnetometer. A typical signal detected from the MTB (measured at 12 mT at 12.6 Hz) and signal recorded from the in-phase field probe are shown. (**F**) Experimental in-phase and out-of-phase susceptibility (left; $n = 3$; means ± SD) and analytical susceptibility data (right). a.u., arbitrary units. (**G**) Schematic of patterned PDMS wells placed in the working space of an MFG-100-i and computational modeling of the magnetic field generated by four NdFeB block magnets. (**H**) Translational velocity of bacteria in the absence and presence of a selection field ($n \geq 6$; mean ± SD; $^{**}P < 0.01$, Student's *t* test).

constant velocity. An estimate of the propulsive force is given by $\boldsymbol{F}_P = \gamma v$, where γ is the linear drag coefficient and v is the linear velocity. For a velocity range of 19 to 49 μm/s (*27*, *28*), the propulsive force is estimated to be on the order of 0.1 pN.

In contrast to DMF, MTB self-propulsion is overridden when subjected to RMF. Viscous drag from the surrounding fluid creates a phase lag between the external field and magnetic moment of the MTB, giving rise to a magnetic torque that is exerted on the bacteria. The opposing hydrodynamic torque (τ_H) that defines the steady-state lag angle between the MTB and magnetic field is governed by $\boldsymbol{\tau}_H = \alpha\omega$, where α is the rotational drag coefficient and the angular frequency (ω) is equal to the frequency of magnetic actuation under synchronous rotation. An estimate of the force generated by this torque-based motion is given by $\frac{\tau_H}{r}$, where r is the distance from the axis of rotation, which is half the bacterial length. For angular frequencies in the range of 10 to 25 Hz at a field magnitude of 20 mT and a distance r of 0.9 μm (fig. S1), the force generated is on the order of 1 pN. These estimates show that, on average, magnetic torque–driven motion generates forces that are an order of magnitude higher than those of MTB self-propulsion. Static field gradients have also been used to pull MTB toward a target site. Although this approach has shown efficacy in small animal models, an impracticable gradient of more than 1300 T/m would be required to produce a comparable force on the same magnetic moment (see Supplementary Text for detailed calculations).

We sought to examine whether the higher forces from torque-based motion produced by RMF can enhance the infiltration of MTB across biological barriers. We first characterized our magnetic control strategy under stringent conditions, using a low field amplitude and a robust cellular barrier. Caco-2 cells cultured on Transwell membranes have been used extensively for the reconstitution of differentiated enterocyte-like monolayers to evaluate oral drug absorption and the translocation of various strains of bacteria (*29*–*31*).

MTB were added to the upper chamber of a Transwell insert with an established Caco-2 monolayer and placed in a polydimethylsiloxane (PDMS) well containing medium. The bacterial concentration in the PDMS well was determined using a hemocytometer after 1 hour of magnetic actuation at 12 mT and 14 Hz using a magnetic field generator (MFG-100-i) consisting of eight electromagnets arranged in a hemisphere. MTB were rotated in plane (parallel) and out of plane (orthogonal) with respect to the cell monolayer and compared with exposure to DMF alone, which was applied along the $-z$ axis (Fig. 2B). Under the stringent conditions of these initial cell monolayer experiments only, a magnetic force generated by spatial variation of the magnitude of the RMF or DMF (1 T/m) was applied along $-z$ to support translocation. The RMF maintained its plane of rotation at all points.

Out-of-plane rotation was found to significantly increase MTB penetration compared with both in-plane RMF and DMF (Fig. 2C). Out of plane actuation for frequencies between 1 and 20 Hz consistently resulted in higher translocation than controls without magnetic exposure (fig. S2). Given these findings, all subsequent experiments were performed using out of plane RMF.

To verify that MTB actuation does not affect monolayer integrity, we performed the Lucifer yellow (LY) rejection assay before and after each experiment. This fluorescent molecule passively diffuses through the cell monolayer by paracellular transport only and, thus, is unable to cross Caco-2 monolayers when tight junctions are well established. LY rejection values remained above 99% under all tested conditions, indicating that no damage occurred to the monolayer (Fig. 2D and fig. S3).

Having observed enhanced MTB translocation using RMF, we investigated the use of RMF for detection of MTB response. Unlike DMF or gradient fields, the time-varying nature of RMF can be exploited for simultaneous actuation and monitoring of MTB, enabling the adjustment of actuation parameters during operation for improved localization and infiltration.

In a proof-of-concept experiment, inductive detection of MTB during actuation was performed using a small-scale, custom-built RMF magnetometer consisting of two pairs of nested Helmholtz coils (Fig. 2E and fig. S4). Phase-shifted sinusoidal currents were applied to each set of coils to produce a circular RMF. When exposed to RMF, the overall magnetic moment of the MTB varies in time by rotating, allowing the measurement of the resulting voltage induced in surrounding loops of wire. Inductive field probes for each pair of coils were placed in the central workspace along with symmetric sense and compensation coils that served to isolate inductive signal from the magnetization of the MTB. After fine-tuning of their cancellation via a potentiometer, the resulting signal was amplified and acquired. The magnetization of the MTB was phase-shifted relative to the rotating field, reflecting the phase lag in the magnetic response of the bacteria.

Using a cosine function fitted to the in-phase field probe, we used integration to separate the acquired signal into in-phase and out-of-phase components of the susceptibility of the sample (Fig. 2F). The experimental data were compared with analytical data to assess whether the detected signal generated by the MTB exhibited predicted characteristics (see the Supplementary Materials). Out-of-phase susceptibility at 12 and 20 mT peaked at 12.6 and 20 Hz, respectively, compared with 14 and 24 Hz in the analytical data. The underlying trends for both in-phase and out-of-phase susceptibility were as predicted by our models, confirming that we were able to detect MTB under actuation with RMF.

Inspired by the gating fields used in magnetic particle imaging (MPI), superimposed magnetostatic fields have recently been demonstrated as a control strategy capable of spatially confining hysteresis heating driven by high-frequency alternating fields (*32*, *33*). By analogy, we have previously suggested that superposition of a static gating field with RMF could also be harnessed for selective actuation of MTB (*25*). The static field suppresses magnetic torque in off-target sites, whereas bacteria near a field-free target region can still undergo full rotation when an RMF is applied. Proof-of-concept experiments were performed in patterned PDMS wells containing suspensions of MTB and a selection field was generated by four block magnets to create a centrally located field-free target well (Fig. 2G). Spatially localized actuation was assessed by measuring torque-induced translational velocity. In the absence of a selection field, comparable translational velocities were observed in all wells, whereas substantial suppression of torque-driven motion was observed in off-target wells when the selection field was applied. Together, these studies illustrate that RMF may offer unique advantages for wirelessly controlled microrobot transport compared with other control strategies, including inductive feedback and spatially selective actuation.

Elucidating the role of torque-driven motion on translocation using computational modeling

Given the prominent effect of RMF on MTB transport across robust cell barriers, we sought to understand the main mechanism driving enhanced translocation using a computational model in COMSOL Multiphysics. Because the endothelium is the first biological barrier encountered after intravenous administration, modeling of transport across a 2D endothelial cell monolayer consisting of adjacent cells forming a sealed barrier between the upper and lower compartments was performed. The cells were modeled as hyperelastic materials with a shear modulus of 1 kPa (*34*, *35*) and dimensions adopted from Arefi *et al.* (*35*). Considering the relative stiffness of Gram-negative bacteria compared with endothelial cells, MTB were modeled as rigid ellipsoids with a rigid dipole moment along the long axis. Transmission electron microscopy images and multisizer data were used to determine the approximate size of a single bacterium, which was estimated to be 0.45 and 1.8 μm for the short and long axes, respectively (fig. S1) (*25*). Hydrodynamic interactions were modeled as linear and rotational viscous damping acting on the rigid body.

Modeling of the forces required for a bacterium to pass through a passive junction yielded estimated contact forces of tens of piconewtons (Fig. 3A). Torque-induced contact force for a bacterium rotating at 14 Hz under 12 mT was shown to be much lower than the resisting force of the cells (Fig. 3B) and the forces required to break bonds formed by vascular endothelial–cadherin (VE-cadherin) (*36*), an endothelial cell–specific adhesion molecule. Buoyant forces and viscous resistance prevent the full conversion of rotational energy into a contact force; thus, the application of forces directly on an endothelial monolayer cannot be the chief mechanism responsible for enhanced translocation. Hence, we sought to examine the influence of translational motion derived from torque-based actuation on bacterial translocation.

Recent work has shown that dynamic mechanical processes within the endothelium result in gap formations that are independent of the influence of migrating cancer or immune cells (*37*, *38*). Using this as a basis, we incorporated stochastic opening of cell-cell contacts into the model to account for the active mechanics of the endothelium. For each simulation, the gap lifetime was set to 160 s (*35*), and a set of random parameters was generated to determine the gap size, which was within the range of 1.5 to 2.5 μm (*34*). The overall simulation time was selected to encompass opening incidences for all gaps. To characterize the permeability of our modeled monolayer, we performed simulations of passive diffusion of liposomes with a diameter of about 200 nm, and 5.9% of the liposomes diffused into the lower compartment (Fig. 3C and movie

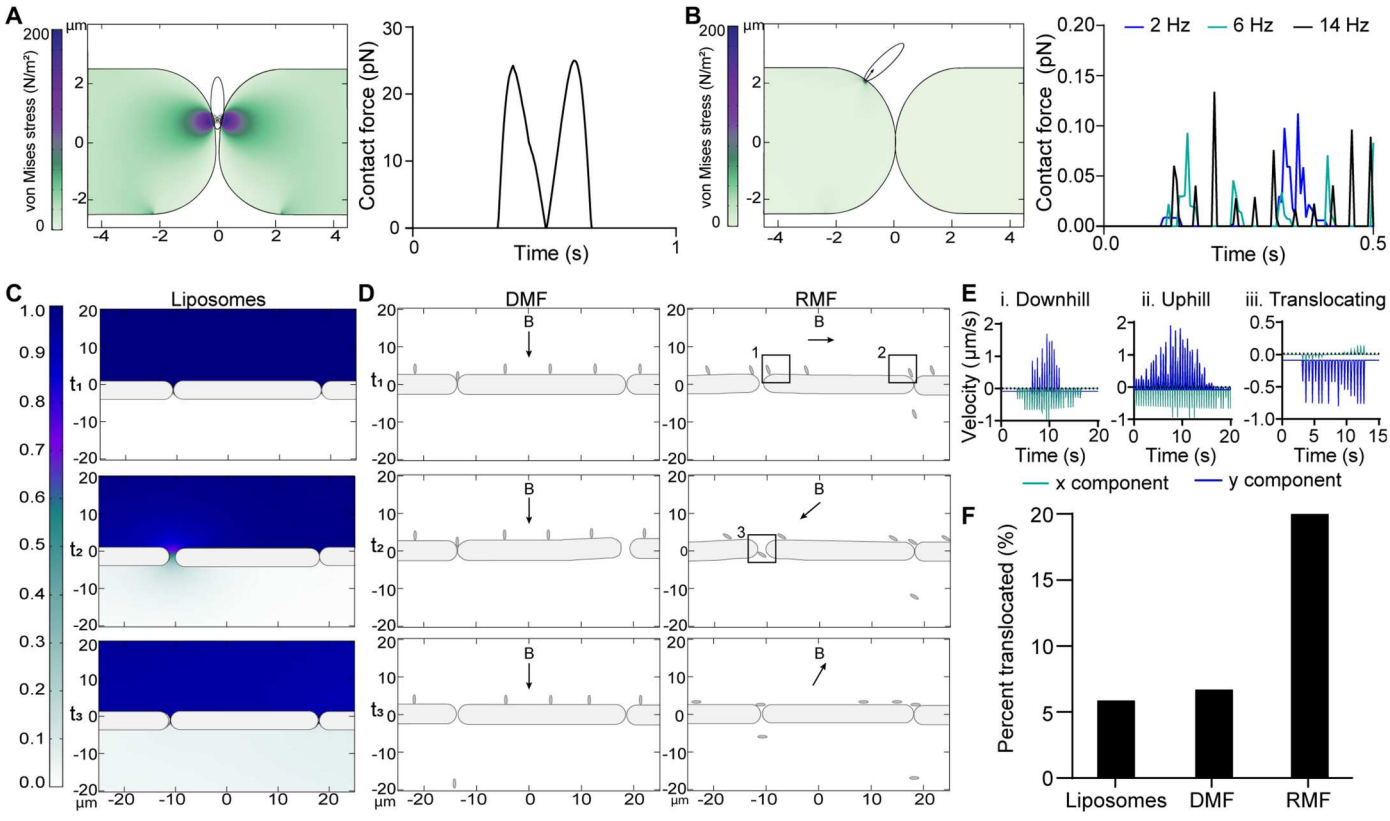

Fig. 3. Computational modeling of MTB transport across endothelial monolayers. (**A**) Modeling of *y*-component contact forces resulting from a single bacterium with prescribed motion successfully transmigrating through a cell junction. (**B**) Model showing discontinuous contact of a rotating bacterium with a cell monolayer. (**C**) Computational simulations of liposome diffusion across a modeled endothelial monolayer. Stochastic opening of cell-cell contacts was incorporated into the model to account for spontaneous gap formation. (**D**) Simulations of MTB transport under DMF and RMF across a modeled endothelial monolayer. (**E**) Velocity profiles showing contributions of the *x* and *y* components of MTB traveling downhill (i), uphill (ii), and translocating through a cell gap (iii). (**F**) Plot of the average amount of liposome diffusion and MTB translocation under DMF and RMF for three simulations relative to the starting concentrations.

S1). Having established the model, we proceeded to compare MTB transport under DMF and RMF (Fig. 3D and movies S2 and S3). The velocity profiles generated for the bacteria under RMF exhibited the well-studied characteristics of surface walkers under low–Reynolds number flows (*39*–*41*) (Fig. 3E). The higher mass density of MTB with respect to the surrounding liquid gives rise to a terminal velocity of the bacteria that results in an offset in the y component of the velocity vector. When traveling along the monolayer, there is discontinuous contact with the surface, and the contributions from the x and y components of the velocity vector vary depending on whether the MTB is traveling downhill or uphill or is translocating. As anticipated, the contribution from the x component is minimal as the MTB passes through an opening, reflecting the lowered contact with the cell surface.

Our model showed that only 6.6% of MTB exposed to DMF crossed the barrier compared with 20% of MTB exposed to RMF (Fig. 3F). Under the static conditions of DMF, the bacteria only passed through the monolayer when initially located in close proximity to a cell-cell junction. In contrast, MTB under RMF translated along the monolayer, which enabled the bacteria to explore the monolayer surface and pass through any gaps that formed between the cells. Overall, these findings strongly suggest that enhanced surface exploration resulting from torque-based translational motion is the dominant mechanism facilitating increased translocation of MTB.

RMF increases extravasation of MTB-liposome conjugates

We proceeded to investigate translocation in an in vitro system suited to model vascular extravasation. Human microvascular endothelial cell (HMEC-1) monolayers cultured on Transwell inserts were used to model the endothelial barriers that would be encountered after intravenous delivery. To verify that intact monolayers were formed when the cells were cultured on permeable membranes, we performed immunostaining for VE-cadherin (Fig. 4A). Confocal imaging showed the presence of intact cell-cell contacts and the formation of a uniform monolayer after 2 days. In an initial experiment, passive diffusion of unconjugated liposomes across the monolayer was measured (fig. S5). From the fluorescence intensity values, it was found that only 0.24% of the liposomes were able to cross into the basolateral chamber via passive diffusion after 1 hour (Fig. 4B).

We then investigated the translocation of MTB-liposome conjugates across the monolayer. The MTB-LP complex combines the adaptability of traditional therapeutic nanocarriers and the functionality of magnetic-based platforms to produce a living microrobot for targeted drug delivery. Bioconjugation of fluorescently labeled liposomes to the MTB cell surface was achieved through carbodiimide-mediated amidation (fig. S6 and table S1). Conjugates were added to the upper chamber of Transwell inserts, and the concentration in the lower chamber was determined after 1 hour of actuation using an MFG-100-i. To increase the available magnetic torque, which is a function of magnetic moment and magnetic field strength, the applied field magnitude was increased to 20 mT. At this field strength, the step-out frequency of our MTB strain of interest was found to be 24 Hz (*25*), in agreement with the magnetometer data (Fig. 2F).

MTB-LP were actuated out-of-plane relative to the monolayer for 1 hour, and this was compared with exposure to DMF and unactuated controls (Fig. 4C). Out-of-plane rotation led to 4.6-fold higher MTB-LP translocation compared with DMF. Exposure to DMF resulted in MTB-LP concentrations that were comparable with unactuated controls, as was the case in the Caco-2 monolayer experiments (Fig. 2C). Transendothelial electrical resistance (TEER) measurements and the LY rejection assay were performed and revealed that MTB actuation does not affect monolayer integrity (Fig. 4, D and E). Both TEER and LY rejection values before and after actuation were comparable, demonstrating that disruption of the monolayer did not occur after exposure to magnetic actuation.

RMF-based control improves MTB transport and colonization of 3D tumor spheroids

Having demonstrated enhanced translocation across endothelial monolayers, we next sought to examine the effect of RMF-based control on MTB-LP tumor penetration in an in vitro tumor model using human breast adenocarcinoma (MCF-7) spheroids. Tumor spheroids can effectively recapitulate the mass transport properties and complex architecture of avascular tumor tissue and have been used to study bacteria-based cancer therapies (*42*–*44*). High levels of E-cadherin expression in MCF-7 cells facilitate the formation of strong cell-cell adhesions particularly in 3D spheroid cultures, making them an ideal model for difficult-to-penetrate tumor masses (*45*). MCF-7 cells transitioned from loose aggregates to highly compact 3D spheroids after 3 days of culture. The spheroids were transferred to PDMS wells, into which conjugates were added. MTB suspensions were stained with a proliferation dye before liposome conjugation to visualize daughter cells over the course of the experiment. After 1 hour of actuation (MFG-100-i, 20 mT and 24 Hz), spheroids were washed thoroughly and incubated for up to 120 hours (Fig. 5A). Given that the results for unactuated controls and DMF were comparable (Figs. 2C and 4C), as well as the lack of a clearly defined preferential direction in a spherical 3D model, RMF was compared with unactuated controls for all subsequent experiments.

Confocal images of live tumors were captured at increments of 10 μm from the bottom of the spheroids to visualize the distribution of 3,3′-dioctadecyloxacarbocyanine perchlorate (DiO)–labeled liposomes after 24 hours of incubation (Fig. 5B). MTB-LP conjugates were able to propel into deep regions of avascular spheroids after exposure to RMF. The density of the conjugate clusters detected in the actuated samples increased with increasing depth. This finding was confirmed by evaluating the mean intensity of each section and compiling a fluorescence distribution for the z plane up to a depth of 100 μm (Fig. 5C). The fluorescence intensity values were consistently higher for actuated samples compared with controls, and peak fluorescence for actuated samples occurred at 80 μm. Decreased signal after 80 μm could be caused by limitations in optical sectioning of deep tissue regions. Given that MTB-LP were mostly located in the center of actuated samples, the high cell density in this region results in tissue opacity, light scattering, and limited light penetration, which restrict visualization of deep tissue sections by confocal microscopy (*46*). Nevertheless, it was still evident that a significantly higher number of conjugates penetrated the spheroids in RMF-exposed samples.

The intensity distribution profiles for the 80-μm sections show distinct differences in the distribution of MTB-LP in actuated samples compared with that in controls (Fig. 5D). Control samples showed a more uniform distribution of the fluorescence signal. In contrast, the overall fluorescence intensity values were

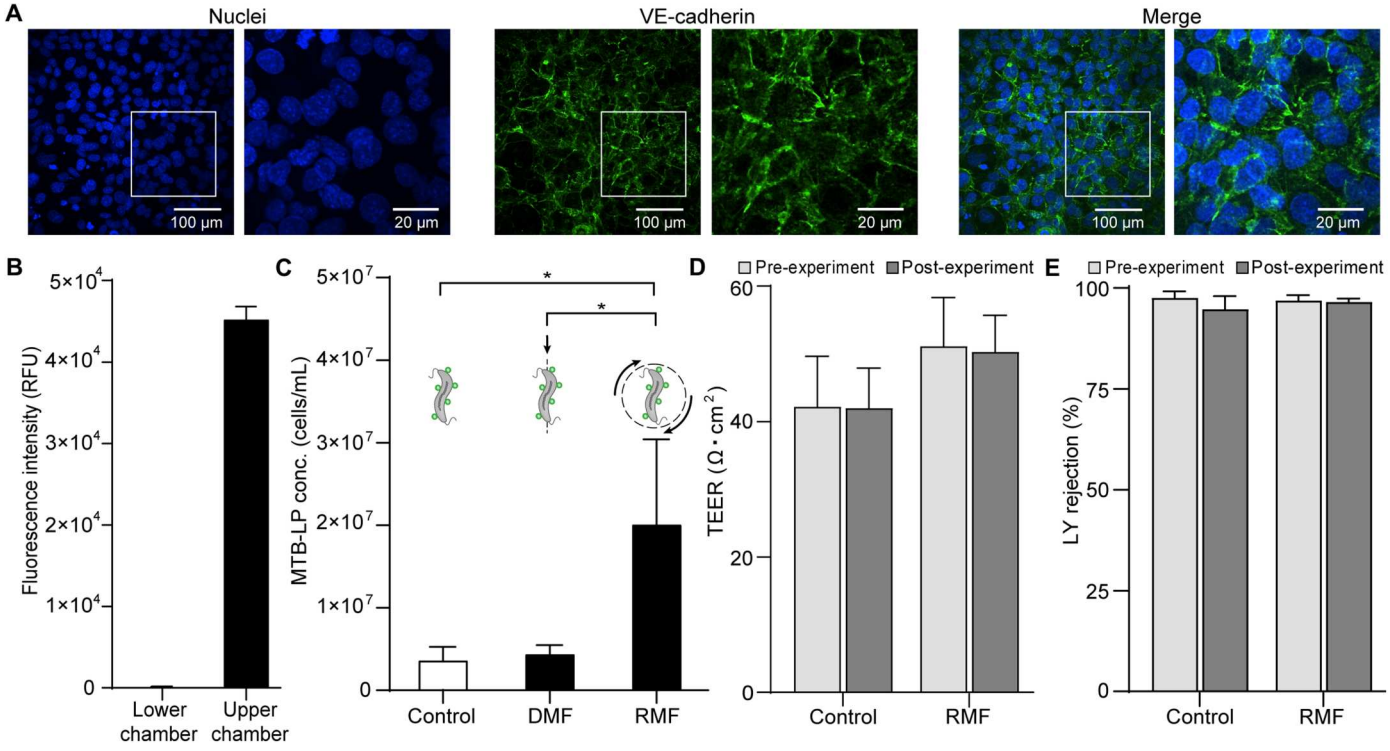

Fig. 4. RMF-based control increases MTB translocation across endothelial monolayers. (**A**) Representative confocal images of immunostaining for VE-cadherin (green) on HMEC-1 cells cultured on a Transwell membrane. Cell nuclei were stained using Hoechst 33342 (blue). (**B**) Evaluation of the lower and upper compartment fluorescence intensity measurements after 1 hour of passive diffusion of liposomes across HMEC-1 monolayers (n = 3; means ± SD). RFU, relative fluorescence units. (**C**) Comparison of lower compartment MTB-LP concentrations after 1 hour for unactuated controls and exposure to either DMF (12 mT) or out of plane RMF (20 mT and 24 Hz) (n = 3; means ± SD; *P < 0.05, ANOVA). No gradients were applied in these experiments. (**D**) Pre- and post-experimental TEER measurements for unactuated controls and out-of-plane RMF (n = 3; means ± SD). (**E**) Pre- and post-experimental LY rejection values for unactuated controls and out of plane RMF (n = 3; means ± SD).

higher in actuated samples, and the fluorescence signal was highest in the central region of the spheroid. A summation of mean fluorescence intensity for each section up to a depth of 100 μm showed that the overall fluorescence intensity, and thus the amount of conjugates delivered in the actuated samples, is fourfold higher than in the controls (Fig. 5E).

Having characterized the efficacy of conjugate delivery using RMF, we were interested in investigating MTB-LP tumor colonization over time. Confocal images of live tumors were used to visualize and quantify the distribution of fluorescently labeled bacteria at 24 and 120 hours for RMF-exposed samples and unactuated controls (Fig. 5F). The z-projection images revealed that MTB were still detectable within the spheroids for both actuated samples and controls after 120 hours. Fluorescence intensity profiles of the spheroids were used to study the localization of the MTB in the spheroids. MTB achieved colonization of the core regions of both actuated and unactuated samples. In addition, there was a narrowing in the intensity profile, indicating an increased density of bacteria at the center of the spheroid from 24 to 120 hours. This enhanced accumulation is likely attributable to autonomous taxis–based navigation. Spheroids over 400 μm in diameter can develop a hypoxic core, and preferential accumulation of MTB in this region might result from oxygen-sensing mechanisms that facilitate their navigation toward hypoxic environments (*47*–*49*).

A summation of mean fluorescence intensity for each section up to a depth of 100 μm was used to assess the relative amount of MTB present in the spheroids at various time points. The fluorescence intensity values in spheroids exposed to RMF were 9.9- and 21.3-fold higher than in the controls at 24 and 120 hours, respectively. The ability of RMF to enhance transport and colonization of MTB was also investigated using HCT116 spheroids (fig. S7). As with MCF-7 spheroids, higher MTB colonization in the core regions of the spheroids was achieved in actuated samples after 120 hours. Over the course of the experiments, the bacteria did not replicate uncontrollably, which is likely a result of the relatively low doubling time of MTB compared with other strains of bacteria. This suggests that some of the risks of infectious complications that have hampered the use of some bacterial strains could be of lower concern (*7*). To overcome the challenges associated with imaging whole spheroids, we performed histological sectioning of MCF-7 spheroids (Fig. 5G). Sections from the center of the spheroids showed that MTB formed clusters between the cells and that there was higher signal from the MTB in spheroids exposed to RMF compared with controls. Overall, these findings indicate that the combination of magnetic torque–driven motion with taxis-based navigation results in robust tumor colonization.

RMF-based control enhances intratumoral transport of MTB in vivo

Motivated by the pronounced effect of RMF on MTB transport in vitro, we next sought to test whether our RMF actuation strategy also enhanced bacterial accumulation in vivo with a pilot study

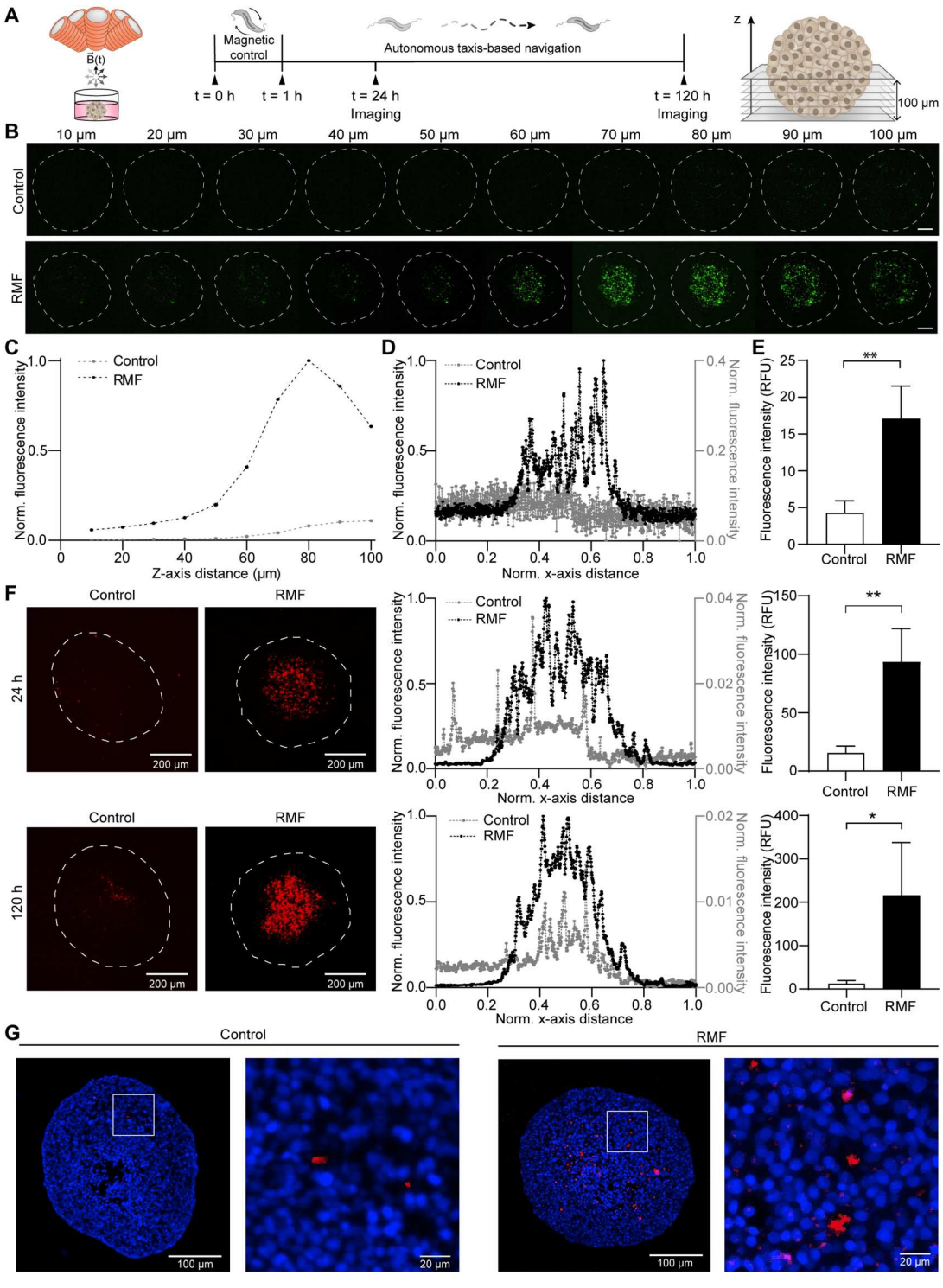

Fig. 5. RMF-based control enhances intratumoral transport of MTB conjugates in 3D tumor spheroids. (**A**) Experimental overview of magnetic actuation followed by taxis and imaging of sequential *z* slices of live tumor spheroids. (**B**) Representative confocal images of live MCF-7 spheroids after 1 hour of exposure to RMF (20 mT and 24 Hz), thorough washing, and 24 hours of incubation. Control refers to unactuated samples. Images were captured at 10-μm increments from the bottom of the spheroids and show the localization of DiO-labeled liposomes (green). Outline depicts the shape of the spheroid at its largest circumference. Scale bars, 100 μm. (**C**) Plot of mean intensity for each section at 10-μm intervals from the bottom of the spheroids along the *z* axis up to a depth of 100 μm. (**D**) Representative fluorescence intensity distribution of the 80-μm section. Values were normalized to overall minimum and maximum fluorescence intensity values. Spheroid diameter was normalized along the *x* axis. (**E**) Summation of mean intensity values for consecutive *z*-plane images up to a depth of 100 μm ($n = 3$; means ± SD; $^{**}P < 0.01$, Student's *t* test). (**F**) Representative *z* projections of MTB stained with a far-red proliferative dye in live MCF-7 spheroids after 1 hour of exposure to RMF (20 mT and 24 Hz), thorough washing, and incubation for up to 120 hours without actuation. Control refers to unactuated samples. Images were captured at 24 and 120 hours. Outline depicts the shape of the spheroid at its largest circumference. Representative normalized fluorescence intensity distribution of actuated samples and controls at 24 and 120 hours. Values were normalized to overall minimum and maximum fluorescence intensity values. Spheroid diameter was normalized along the *x* axis. Image-based quantification of fluorescence intensity values from *z* projections at 24 and 120 hours (right; $n = 3$; means ± SD; $^{*}P < 0.05$ and $^{**}P < 0.01$, Student's *t* test). (**G**) Representative images of 5-μm histology sections for MCF-7 spheroids 144 hours after actuation.

using a mouse model. BALB/c nude mice bearing subcutaneous MCF-7 tumors in one hind flank received intravenous injections of 1×10^9 MTB stained with a far-red proliferative dye (Fig. 6A). Previous studies used peritumoral administration of MTB and applied static magnetic fields to direct bacteria away from the injection site toward the tumor (*21*, *22*). Here, we used systemic administration where a directing magnetic field cannot be meaningfully applied at the tumor site. Hence, for this experiment, anesthetized mice were placed either in the absence of magnetic actuation (control) or with tumors positioned in the workspace of an MFG-100-i applying a 20-mT RMF at 14 Hz for 1 hour. For an applied field magnitude of 20 mT, uniform fields with negligible offset gradients are expected within the workspace of the field generator (Fig. 6B and fig. S8), ensuring that the observed effects on the accumulation of bacteria can solely be attributed to the rotational character of the applied field.

After treatment, mice were returned to the cage for 24 hours, after which the tumor and major organs were harvested to assess

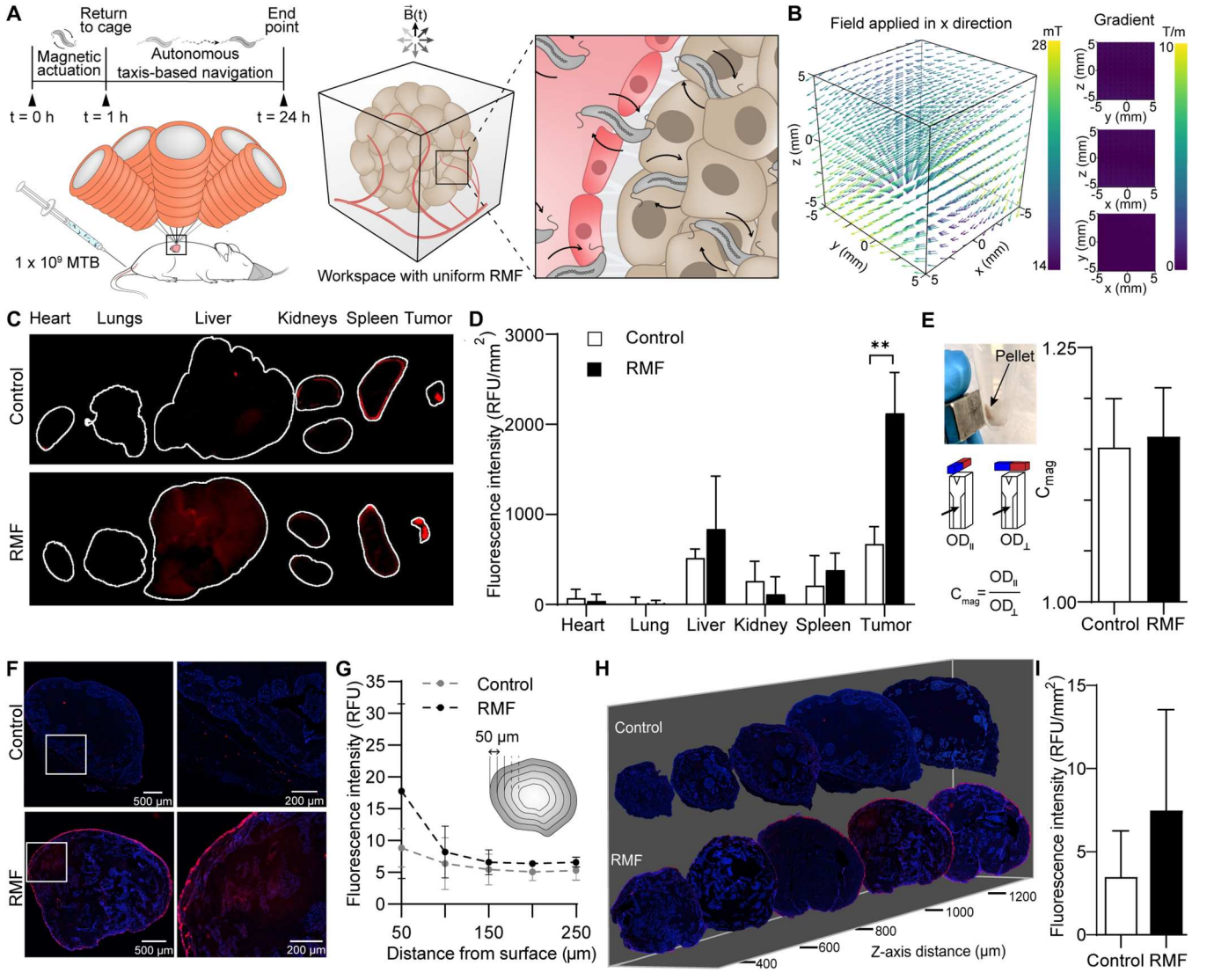

Fig. 6. Assessment of intratumoral transport of MTB in vivo. (**A**) BALB/c nude mice bearing subcutaneous MCF-7 tumors in one hind flank were intravenously administered with 1×10^9 MTB stained with a far-red proliferative dye. The mice were anesthetized for 1 hour in the absence of exposure to magnetic actuation (control) or were placed on a magnetic field generator with tumors positioned in the workspace (RMF). Mice were returned to the cage for 24 hours, after which the tumor and major organs were harvested for further analysis. (**B**) Plots of expected field magnitude and gradients produced in the workspace of the magnetic field generator for an applied field of 20 mT in the *x* direction. (**C**) Representative fluorescence intensity images of harvested organs and tumors 24 hours after injection of far-red stained MTB. (**D**) Quantitative biodistribution from harvested organs and tumors ($n = 3$; means ± SD; $^{**}P < 0.01$, Student's *t* test). (**E**) Representative image of magnetically responsive pellet and C_{mag} values for homogenized tumors placed in liquid culture for 8 days ($n = 3$, control; $n = 4$, RMF; means ± SD). (**F**) Representative images of 10-µm histology sections that were sectioned at a depth of about 1 mm in the tumor. Cell nuclei were stained using Hoechst 33342 (blue). (**G**) Mean intensity values with increasing distance from the periphery of the tumor sections for the first 250 µm of each slice ($n = 3$; means ± SD). (**H**) Representative transverse tumor sections. The *z* axis denotes the approximate position of consecutive slices with respect to the surface of the tumor. Cell nuclei were stained using Hoechst 33342 (blue). (**I**) Summation of mean intensity values for consecutive traverse tumor sections ($n = 3$; means ± SD).

the distribution of the bacteria using a whole-organ fluorescence scanner (Fig. 6C). Fluorescence signal was detected in all tumors, suggesting that the bacteria innately accumulated in tumors. This signal was 3.16-fold higher in mice with tumors exposed to RMF compared with unactuated controls (Fig. 6D). Very low signals were detected in most of the major organs except for the liver, consistent with previous findings 24 hours after intravenous administration of this bacterial strain (*50*). Bacterial accumulation in the liver is expected to decrease over time, with full clearance by day 6 (*50*).

To assess whether the bacteria detected in the fluorescence scans were still viable, harvested tumors were homogenized and placed into MTB culture medium. After 8 days, large, dark pellets that were magnetically responsive were present in all tubes, indicating that the tumor homogenates contained live MTB (Fig. 6E). C_{mag} measurements were performed to quantify the magnetic properties of the cultures, and all samples had values above 1, signifying magnetic responsiveness of the bacterial suspensions.

Histological sectioning of the tumors was performed, with sections collected at a depth of about 1 mm in the tumor showing more pronounced accumulation at the periphery in both control and actuated samples (Fig. 6F). Mean intensity distributions with increasing distance from the periphery for the tumor section show that bacteria can be detected throughout the first 250 μm of each slice, with higher overall signal from samples exposed to RMF compared with controls (Fig. 6G). Transverse histology sections were also compiled and evaluated to assess the distribution of MTB with increasing distance from the surface of the tumor (Fig. 6H). Summation of the mean fluorescence intensity for consecutive transverse tumor sections showed that the overall fluorescence intensity, and thus the amount of MTB delivered in the actuated samples, was 2.1-fold higher than in the controls (Fig. 6J). These results, combined with the findings from our in vitro analysis, demonstrate the potential of magnetic torque–driven control strategies for enhanced tumor accumulation.

DISCUSSION

Biohybrid microrobots, when combined with scalable control strategies, have the potential to enhance tumor colonization, substantially improving prospects for the clinical translatability of bacterial cancer therapy. Efforts to enhance the accumulation of magnetically responsive, therapeutic agents using magnetic fields have most often relied on powerful static field gradients to draw the drug carriers toward a target site (*51*–*53*). This approach has intrinsic limitations that narrow its potential for clinical translation. Magnetic fields decrease with the cube of the distance from a dipole, and their gradients diminish even more rapidly. This implies that the length scales associated with many tumors would require sources with impracticable field strengths. In contrast, uniform RMF can be generated at clinically relevant scales for open-loop control of magnetically responsive agents in deeply situated tumors.

The time-varying character of RMF presents the opportunity for simultaneous actuation and detection of living magnetic microrobots. Our proof-of-concept experiments established that MTB actuated with RMF can be inductively detected and that their torque-based motion can be suppressed in off-target regions by a magnetostatic gating field. These demonstrations lay a foundation for further development of spatially confined actuation, simultaneous monitoring, and closed-loop optimization of driving parameters. In vivo inductive detection of magnetic tracers driven with alternating magnetic fields has already been widely investigated with MPI (*54*). The possibility for concurrent imaging and actuation with MPI has also been recognized, combining particle tracking of superparamagnetic iron oxide nanoparticles with cancer hyperthermia in vivo (*32*). Gradient fields used in MPI have proven challenging to scale up to humans, but recent efforts have demonstrated MPI in deep regions in human brains with moderate resolution (*55*). One foreseeable challenge to simultaneous inductive monitoring and actuation of MTB with RMF is that frequencies of tens of hertz are used rather than the kilohertz signals generated in MPI, resulting in correspondingly weaker inductive signals. Another is that the lack of higher-order harmonics contributed to the inductive signal with rotational actuation, which arises in MPI from periodic saturation of the magnetic tracers. Future work will need to identify strategies to overcome these obstacles.

Magnetic torque–driven motion, followed by autonomous taxis–based navigation, proved to be a highly effective hybrid control strategy for enhanced transport of living microrobots across various biological barriers. MCF-7 spheroids were used to model avascular tumor tissue, Caco-2 monolayers were used to generate a model for a robust cellular barrier, and HMEC-1 monolayers were used to model the vascular endothelium. In both monolayer models, translocation driven by the application of an RMF significantly outperformed the DMF and unactuated controls (Figs. 1B and 3C). Computational modeling showed that torque-driven translational motion, which led to increased cell surface exploration, was the primary mechanism responsible for increasing transport across monolayers. Although not the chief mechanism driving MTB-LP transport, shear forces exerted by rotating MTB-LP on the cell surface may still contribute, in part, to higher transport across monolayers and increased accumulation in spheroids. The heterogeneity of MTB populations may allow a small subset of bacteria with especially high magnetic moments to exert sufficient forces on mechanotransducers, such as VE-cadherin and E-cadherin. This can trigger responses including transient disruptions of intercellular junctions (*56*, *57*). Combined with the translation of the bacteria on the cell surface, these relatively rare disruptions could assist in enhancing local permeability and transport of MTB-LP.

We also showed that the results from the in vitro characterization of our open-loop control strategy can be replicated in the highly complex biological environment in vivo. We have demonstrated that significant accumulation of systemically administered MTB can be achieved for tumors exposed to RMF. Previous studies using magnetic control after peritumoral administration have shown considerable bacterial accumulation (*21*, *22*). However, this route of administration is limited to easily accessible tumors, which raises the barrier for practical clinical use. In choosing systemic administration, we demonstrate the robustness of our strategy for improved delivery of bacterial microrobots despite stochastic distribution of the injected dose and the added barriers posed by clearance mechanisms present in the circulatory system. Given that this strain of MTB remains viable after intravenous injection, future studies can incorporate longer time points to facilitate the study of taxis-based accumulation in tumor cores, as well as further bacterial clearance from off-target sites.

Combining this control strategy for increased infiltration of bacterial microrobots with therapeutic delivery could potentially be a

powerful tool for improving the efficacy of bacteria-mediated therapy. Imparting magnetic responsiveness to more commonly used bacterial species, such as *Escherichia coli* (*58*), is of increasing interest in the field of bacterial cancer therapy. This approach could allow for more effective use of such strains, improving both safety and efficacy. Strategies to achieve this include surface functionalization using magnetic nanoparticles or genetic engineering, which is supported by insights into the genes involved in the process of biomineralization in MTB for transfer into nonmagnetic species (*59*). By merging the benefits of bacteria-mediated therapy with a scalable magnetic torque–driven control strategy, our approach enables effective, targeted delivery of living microrobots for improved cancer treatment.

MATERIALS AND METHODS

Materials

Human colorectal adenocarcinoma [Caco-2; American Type Culture Collection (ATCC), HTB-37], human microvascular endothelium (HMEC-1; ATCC, CRL-3243), human breast adenocarcinoma (MCF-7; ATCC, HTB-22), human colorectal carcinoma (HCT116; ATCC, CCL-247), *M. magneticum* (ATCC, 700264), Wolfe′s vitamin solution, and Wolfe′s mineral solution were purchased from ATCC (Manassas, VA). 1,2-Dipalmitoyl-*sn*-glycero-3-phosphocholine (DPPC) and 1,2-distearoyl-*sn*-glycero-3-phosphoethanolamine-*N*-[carboxy(polyethylene glycol)-2000] (sodium salt) (DSPE-PEG2000-COOH) were purchased from Avanti Polar Lipids Inc. (Alabaster, AL). Penicillin/streptomycin (P/S) was purchased from Corning (Corning, NY), fetal bovine serum (FBS) was purchased from BioWest (Nuaillé, France), 1-ethyl-3-[3-(dimethylamino)propyl]-carbodiimide (EDC) was purchased from TCI EUROPE (Eschborn, Germany), and Hoechst 33342 was purchased from Invitrogen (Burlington, CA). Calcein and 4% formaldehyde (Histofix 4%) were purchased from Carl Roth (Karlsruhe, Germany). VE-cadherin rabbit monoclonal primary antibody and Alexa Fluor 488-conjugated anti-rabbit immunoglobulin G (IgG) secondary antibody were obtained from Cell Signaling Technology (Danvers, MA). Potassium phosphate, succinic acid, tartaric acid, sodium nitrate, ascorbic acid, sodium acetate, resazurin sodium salt, gelatin, epidermal growth factor (EGF), hydrocortisone, Hanks′ balanced salt solution (HBSS), dimethyl sulfoxide (DMSO), LY CH dipotassium salt, sepharose CL-2B, bovine serum albumin (BSA), DiO, phosphate-buffered saline (PBS), Triton X-100, resazurin, and *N*-hydroxysulfosuccinimide (sulfo-NHS) were all acquired from Sigma-Aldrich (St. Louis, MO). Dulbecco′s modified Eagle′s medium (DMEM), McCoy′s 5A medium, L-glutamine, CellTrace Far-Red cell proliferation kit, agarose, and MCDB131 medium were acquired from Thermo Fisher Scientific (Waltham, MA).

Mammalian cell culture

Caco-2 cells were cultured in high-glucose DMEM supplemented with 20% FBS and 1% P/S. HMEC-1 cells were cultured in MCDB131 supplemented with 10% FBS, 1% P/S, 10 mM L-glutamine, hydrocortisone (1 μg/ml), and EGF (10 ng/ml). MCF-7 cells were cultured in high-glucose DMEM supplemented with 10% FBS and 1% P/S. HCT116 cells were cultured in McCoy′s 5A medium supplemented with 10% FBS and 1% P/S. All cell lines were incubated at 37°C with 5% CO_2 in a humidified atmosphere. Cells were harvested at 80% confluency, and cell density was determined using a hemocytometer. The required number of cells was seeded for each experiment as specified. One day before experiments, medium was replaced with antibiotic-free medium.

Bacteria culture

Cultures of *M. magneticum* strain AMB-1 were grown in revised magnetic spirillum growth medium (MSGM; ATCC, Medium 1653) that contained the following per liter of distilled water: 5.0 ml of Wolfe′s mineral solution, 0.45 ml of 0.1% reasazurin, 0.68 g of potassium phosphate, 0.37 g of succinic acid, 0.37 g of tartaric acid, 0.12 g of sodium nitrate, 0.035 g of ascorbic acid, and 0.05 g of sodium acetate. The final pH was adjusted to 6.75 with 1 M NaOH before autoclaving. Before use, Wolfe′s vitamin solution (1000×) and 10 mM ferric quinate (200×) were added to the culture medium. Incubation occurred anaerobically at 30°C, and cultures were passaged every 5 to 7 days.

Caco-2 monolayer culture and permeability assay

Caco-2 cells were seeded at a density of 1×10^5 cells/cm^2 on 12-well Transwell inserts (3.0-μm pore size; Corning). Cells were cultured on the inserts for 16 to 21 days, and medium was exchanged every second day. An LY paracellular permeability assay was performed to determine the integrity of the established Caco-2 monolayer. Before and after each assay, cell monolayers were washed three times with HBSS. The basolateral compartment of a well plate was filled with 1.5 ml of 1% DMSO in HBSS, and 0.5 ml of LY (1 mg/ml) in 1% DMSO/HBSS was added to the apical compartment. After 1 hour of incubation at 37°C, the fluorescence intensity of the solutions from the apical and basolateral compartments were measured at 485/535 nm using a Spark multimode microplate reader (Tecan). The percent rejection of LY was calculated as follows:

$$\%\text{Lucifer yellow rejection} = 100 \times \left[1 - \frac{\text{FI}_{\text{basolateral}}}{\text{FI}_{\text{apical}}}\right] \quad (1)$$

where FI is fluorescence intensity.

Transwell inserts with an LY rejection value greater than 99% were used for further experiments. After each experiment, the LY assay was repeated to confirm that the integrity of the monolayer was maintained.

Integrated imaging and wireless magnetic control platform

A small-scale arbitrary magnetic field generator consisting of eight electromagnets arranged in a single hemisphere was used to apply RMF (MFG-100-i, MagnebotiX, Zürich, Switzerland). The system was integrated with an inverted spinning disk confocal microscope (Nikon Eclipse Ti2 with Yokogawa CSU-W1 unit and Hamamatsu C13440-20CU Digital CMOS camera), which was used for all imaging. Samples were positioned between the objective lens and the hemisphere of the electromagnets.

MTB translocation across Caco-2 cell monolayers

Transwell inserts with Caco-2 monolayers were placed into PDMS wells (Ø = 22 mm) containing 1.5 ml of medium. MTB at a concentration of 1×10^8 MTB/cm^2 were added to the apical chamber, and samples were exposed to either a DMF of 12 mT or a localized RMF of 12 mT with frequencies between 1 and 20 Hz. A magnetic force generated by the superposition of moderate gradients of 1 T/m was

applied along $-z$. After 1 hour, the bacteria concentration in the basolateral chamber was determined by live counting in a hemocytometer. Bacteria concentrations for actuated samples were normalized to unactuated controls.

Inductive detection of MTB

Inductive detection of MTB was performed using a custom-built RMF magnetometer. Two pairs of nested Helmholtz coils were wound using enamel-coated copper wire (Ø = 0.8 mm) and housed in a 3D printed frame (fig. S4). The inner set of coils contained 256 turns of wire, and the outer coils consisted of 265 turns. Phase-shifted sinusoidal signals were generated (Digilent Analog Discovery 2) and amplified (Crown D-150A Series II), resulting in a sinusoidal waveform in each set of Helmholtz coils to produce a circular RMF. Inductive field probes for each pair of coils were placed in the central workspace along with sense and compensation coils. Signals from the sense and compensation coils underwent differential amplification, and the residual signal from the magnetized sample was acquired with an oscilloscope (Keysight DSOX2004A). All samples contained 100 μl of MTB at about OD_{600} (optical density at 600 nm) = 1.5, suspended in MSGM. Measurements were collected at field amplitudes of 12 and 20 mT at a frequency range between 12 and 80 Hz. A detailed description of the setup and the associated data processing pipeline can be found in the Supplementary Materials.

Spatially selective actuation of MTB

Selection field experiments were performed in square PDMS devices featuring five patterned wells (Ø = 3 mm). NdFeB block magnets (5 mm by 2.5 mm by 1.5 mm; Supermagnete) were placed with arbitrarily defined north poles facing inward on the east and west faces of the device, whereas magnets with south poles facing inward were positioned on the remaining faces. This generated a gating field with a centrally located zero point. Each well was filled with an MTB suspension of OD_{600} = 1.2, and translational velocity with and without a magnetostatic gating field was measured when an RMF of 12 mT and 14 Hz was applied.

Computational model of endothelial translocation

A numerical simulation in COMSOL Multiphysics (version 5.5) was implemented to study the translocation of microstructures across an endothelial barrier under different conditions. MTB were modeled as rigid ellipsoids with a magnetic dipole moment using dimensions obtained from multisizer data. Endothelial cells were modeled as hyperelastic materials, and stochastic opening of cell-cell contacts was incorporated to model dynamic gap formation that occurs in endothelial cell monolayers. The effect of the surrounding fluid was modeled through linear and rotational drag coefficients assuming Stokes flow regime. A time-varying external magnetic field was applied, and this was balanced with forces and torques arising from hydrodynamic and mechanical interactions with the viscous fluid and adjacent substrate. Further details can be found in the Supplementary Materials.

Liposome preparation and characterization

Fluorescently labeled carboxylated liposomes were prepared from a total of 14 μmol of lipids using thin-film hydration. For imaging, DPPC, DSPE-PEG2000-COOH [5 mole percent (mol %)], and DiO (0.5 mol %) were combined in 0.5 ml of chloroform and dried to a thin film under nitrogen with further vacuum desiccation overnight at room temperature. The lipid thin film was hydrated with 1 ml of PBS and placed in a water bath for 1 hour at 50°C with continuous stirring. Liposomes were downsized using sequential extrusion on a heating block (Avanti) at 50°C. Liposomes were passed 21 times each through a 400-nm followed by a 200-nm polycarbonate membrane (Whatman). For flow cytometry, DPPC and DSPE-PEG2000-COOH (5 mol %) were combined to form a thin film as previously described. The film was rehydrated with 1 ml of calcein solution (35.2 mM) and downsized as described. Unencapsulated calcein was removed by size exclusion chromatography using a Sepharose CL-2B column. The average diameter, size distribution, and zeta potential of the liposomes were determined by dynamic light scattering (Litesizer 500, Anton Paar).

MTB staining and covalent coupling of liposomes

MTB cells at a concentration of 1.5×10^8 cells/ml in PBS were stained using the CellTrace Far-Red cell proliferation kit. A stock solution was prepared according to the manufacturer's protocol, and 2 μl was added to the MTB suspension. Cells were incubated at room temperature for 20 min and protected from light with gentle agitation. After incubation, 10 μl of 1% BSA was added to the cell suspension for 5 min to remove free dye. Cells were pelleted and resuspended in PBS.

Bioconjugation was then achieved through carbodiimide coupling using an adapted protocol (*60*). Briefly, activation of carboxylated liposomes was accomplished by incubating 300 μl of liposome solution with EDC and sulfo-NHS (EDC/NHS/DSPE-PEG2000-COOH = 30:30:3, mol/mol) for 20 min in PBS (pH 5.5) at room temperature with gentle agitation. The activated liposomes were subsequently incubated with 1.5×10^8 MTB cells for 2 hours at room temperature with gentle agitation. Unbound liposomes were separated from MTB-liposome conjugates (MTB-LP) using a 2D magnetic field, and the sample was redispersed in PBS (pH 7.4).

Quantification of liposome binding by flow cytometry

For quantitative analysis of liposome binding, MTB-LP conjugates were analyzed using flow cytometry (BD LSRFortessa) with a 488-nm excitation laser and 530/30 filter. Untreated MTB cells and unbound liposomes were used as controls, and the fluorescence emission of 10,000 events was recorded. Data were analyzed using FlowJo (Tree Star), and appropriate gates and controls were used to generate density plots and histograms of each sample.

HMEC-1 monolayer culture and immunofluorescence staining

HMEC-1 cells were seeded at a density of about 1×10^5 cells/cm^2 on 12-well Transwell inserts (3.0-μm pore size) and cultured on the inserts for 2 days. HMEC-1 monolayers were fixed in 4% paraformaldehyde for 15 min and permeabilized in 0.1% Triton X-100 for 10 min at room temperature. Fixed cells were blocked with 1% BSA in PBS for 1 hour, followed by overnight incubation at 4°C with a VE-cadherin rabbit monoclonal primary antibody (diluted 1:500 in blocking buffer). The monolayers were then incubated for 1 hour at room temperature in an Alexa Fluor 488-conjugated anti-rabbit IgG secondary antibody (diluted 1:1000 in blocking buffer). Staining for DNA was performed with Hoechst 33342. Monolayers were incubated in Hoechst 33342 at a final concentration of 10 μg/ml in

PBS for 10 min at room temperature. The membranes were then detached from the Transwell inserts, mounted on glass coverslips, and imaged.

Translocation across HMEC-1 cell monolayers

HMEC-1 monolayers cultured on Transwell inserts were placed into PDMS wells (Ø = 22 mm) containing 1.5 ml of medium. MTB-LP at a concentration of 1×10^8 MTB-LP/cm^2 was added to the apical chamber and exposed to either a DMF of 12 mT or a localized RMF of 20 mT and 24 Hz. After 1 hour, the concentration and size distribution of MTB-LP in the basolateral chamber were determined using a multisizer (4e Coulter Counter, Beckman Coulter). For comparison, liposomes were added to monolayers at a concentration corresponding to the liposomes on the conjugates. After 1 hour, the solutions from the apical and basolateral compartments were collected and measured at 485/535 nm using a Spark multimode microplate reader (Tecan).

Before and after each assay, LY rejection (as previously described) and TEER measurements were performed using the EVOM3 Volt/Ohmmeter (World Precision Instruments). TEER was calculated using the equation

$$\mathrm{TEER} = (R_{\mathrm{total}} - R_{\mathrm{blank}}) \times A \quad (2)$$

where R_{total} is the measured resistance from a Transwell insert with a cultured monolayer, R_{blank} is the resistance of a Transwell insert without a monolayer, and A is the area of Transwell insert (1.12 cm^2).

MCF-7 spheroid formation and staining

MCF-7 tumor spheroids were formed and cultured in 96-well ultralow adhesion plates (Corning). Cells were seeded at a density of 10,000 cells per well in 100 μl of medium. The well plates were centrifuged at 1000*g* for 10 min and incubated in a humidified atmosphere with 5% CO_2 at 37°C. Tumor spheroids grew to about 500 μm in diameter after 3 days. Before experiments, staining for DNA was performed with Hoechst 33342. Spheroids were incubated for 1 hour at 37°C with Hoechst 33342 at a final concentration of 5 μg/ml in medium.

MTB-LP accumulation in MCF-7 spheroids

MCF-7 spheroids were transferred to PDMS wells (Ø = 6 mm) containing 5×10^7 MTB-LP in 100 μl of medium. Spheroids were subsequently imaged under magnetic actuation at 20 mT and 24 Hz. After 1 hour, spheroids were washed thoroughly with PBS and incubated in ultralow adhesion well plates for up to 144 hours at 37°C with 5% CO_2 in a humidified atmosphere.

Quantification of MTB-LP accumulation in MCF-7 spheroids

Analysis and processing of captured image stacks was performed in ImageJ (National Institutes of Health). For each spheroid, a summation of consecutive *z*-plane images in the first 100 μm was performed for each time point (fig. S9A). Regions of interest (ROIs) were defined using the Hoechst image stack by tracing a contour around the spheroid at 0 and 100 μm. Intermediate ROIs were defined using interpolation, with about 3-μm radial increments (fig. S9B). These ROIs were then applied to the corresponding DiO liposome image stack, and fluorescence intensity measurements were performed. Fluorescence values were normalized to the fluorescence of the surrounding medium (fig. S9C).

To generate fluorescence intensity distributions at a depth of 80 μm, we defined rectangular ROIs at the boundaries of the spheroid. The average pixel intensity values along the *x* axis were normalized to the minimum and maximum intensity across all the spheroids to allow comparison, using the following equation:

$$\text{Norm. fluorescence intensity} = \frac{\text{Ave. intensity} - \text{Min. intensity}}{\text{Max. intensity} - \text{Min. intensity}} \quad (3)$$

Normalized fluorescence intensity was plotted against the normalized *x* axis distance to obtain the MTB-LP distribution in the spheroids.

In vivo magnetic actuation experiments

All animal experiments were approved and performed in accordance with the guidelines from Veterinamäramt Kanton Zürich under licence number ZH151/2020 and laboratory animal husbandry number 159. Female BALB/c nude mice (6 to 8 weeks; Charles River Laboratories) were acclimatized for 3 weeks and inoculated subcutaneously in the hind flank with 5×10^6 MCF-7 cells suspended in Matrigel (8 mg/ml) at a volume of 100 μl. When tumor diameters exceeded 5 mm, mice were blindly randomized into various groups with a minimum of three mice per group. Tail-vein (intravenous) injections of MTB stained with a far-red proliferative dye were administered at a concentration of 1×10^9 in 100 μl of PBS. Mice were placed under anesthesia in the absence of magnetic actuation (control) or with tumors positioned in the workspace of the magnetic field generator and exposed to actuation at 20 mT and 14 Hz for 1 hour (RMF). Mice were then returned to the cage for 24 hours, after which the mice were euthanized and the tumor and major organs were harvested. For semiquantitative biodistribution analysis, far-red fluorescence signals were measured using an ex vivo fluorescence imaging system (Sapphire Biomolecular Imager, Azure Biosystems).

Harvested tumors were weighed and homogenized using a gentleMACS tissue dissociator (Miltenyi Biotec) (C tubes) before being cultured for 8 days under the MTB culture conditions described previously. C_{mag} measurements were performed to quantify the magnetic responsiveness of the samples. OD_{600} was measured with a magnet placed parallel ($OD_{||}$) and then perpendicular ($OD_{⊥}$) to the light path. The C_{mag} value was calculated as the fraction of $OD_{||}$ and $OD_{⊥}$.

Histology

Spheroids, incubated for 144 hours after experiments, and harvested tumors were fixed in 4% formaldehyde for 1 hour and washed three times with PBS. For spheroids, a 5% (w/v) agarose solution in deionized (DI) water was mixed with a 5% (w/v) solution of gelatin at a 1:1 ratio, and the fixed spheroids were embedded in the resulting hydrogel. After dehydration in graded alcohol and isoparaffin (LOGOS J, Milestone Medical), spheroid-containing hydrogels or tumors were embedded in paraffin, and sections of 5 to 10 μm were cut using a microtome (HM 355S, Microm AG). The sections were stained with Hoechst 33342 at a concentration of 5 μg/ml in DI water, and the slides were mounted and imaged.

Statistical analysis

All values are expressed as the means ± SD of at least three replicates, unless otherwise stated. Statistical analysis between two groups was performed using an unpaired Student's *t* test, and for comparisons of more than two groups, analysis of variance (ANOVA) with Tukey's post hoc analysis was performed. A $P < 0.05$ was considered statistically significant. Plotting of graphs and statistical analysis were performed using GraphPad Prism 8.0 software.

Supplementary Materials

This PDF file includes:
Supplementary Text
Figs. S1 to S9
Table S1
References (*61*–*67*)

Other Supplementary Material for this manuscript includes the following:
Movies S1 to S5

REFERENCES AND NOTES

1. J. W. Yoo, D. J. Irvine, D. E. Discher, S. Mitragotri, Bio-inspired, bioengineered and biomimetic drug delivery carriers. *Nat. Rev. Drug Discov.* **10**, 521–535 (2011).
2. D. Akin, J. Sturgis, K. Ragheb, D. Sherman, K. Burkholder, J. P. Robinson, A. K. Bhunia, S. Mohammed, R. Bashir, Bacteria-mediated delivery of nanoparticles and cargo into cells. *Nat. Nanotechnol.* **2**, 441–449 (2007).
3. S. Chowdhury, S. Castro, C. Coker, T. E. Hinchliffe, N. Arpaia, T. Danino, Programmable bacteria induce durable tumor regression and systemic antitumor immunity. *Nat. Med.* **25**, 1057–1063 (2019).
4. F. Avogadri, C. Martinoli, L. Petrovska, C. Chiodoni, P. Transidico, V. Bronte, R. Longhi, M. P. Colombo, G. Dougan, M. Rescigno, Cancer immunotherapy based on killing of *Salmonella*-infected tumor cells. *Cancer Res.* **65**, 3920–3927 (2005).
5. C. H. Lee, C. L. Wu, A. L. Shiau, Toll-like receptor 4 mediates an antitumor host response induced by *Salmonella choleraesuis*. *Clin. Cancer Res.* **14**, 1905–1912 (2008).
6. N. S. Forbes, Engineering the perfect (bacterial) cancer therapy. *Nat. Rev. Cancer* **10**, 785–794 (2010).
7. S. Felgner, D. Kocijancic, M. Frahm, S. Weiss, Bacteria in cancer therapy: Renaissance of an old concept. *Int. J. Microbiol.* **2016**, 8451728 (2016).
8. F. Heppner, J. R. Möse, The liquefaction (oncolysis) of malignant gliomas by a non pathogenic Clostridium. *Acta Neurochir.* **42**, 123–125 (1978).
9. J. F. Toso, V. J. Gill, P. Hwu, F. M. Marincola, N. P. Restifo, D. J. Schwartzentruber, R. M. Sherry, S. L. Topalian, J. C. Yang, F. Stock, L. J. Freezer, K. E. Morton, C. Seipp, L. Haworth, S. Mavroukakis, D. White, S. MacDonald, J. Mao, M. Sznol, S. A. Rosenberg, Phase I study of the intravenous administration of attenuated *Salmonella typhimurium* to patients with metastatic melanoma. *J. Clin. Oncol.* **20**, 142–152 (2002).
10. D. L. Lamm, BCG immunotherapy for transitional-cell carcinoma in situ of the bladder. *Oncology (Williston Park)* **9**, 947–952 (1995).
11. S. Zhou, C. Gravekamp, D. Bermudes, K. Liu, Tumour-targeting bacteria engineered to fight cancer. *Nat. Rev. Cancer* **18**, 727–743 (2018).
12. A. Sahari, M. A. Traore, B. E. Scharf, B. Behkam, Directed transport of bacteria-based drug delivery vehicles: Bacterial chemotaxis dominates particle shape. *Biomed. Microdevices* **16**, 717–725 (2014).
13. E. Steager, C. B. Kim, J. Patel, S. Bith, C. Naik, L. Reber, M. J. Kim, Control of microfabricated structures powered by flagellated bacteria using phototaxis. *Appl. Phys. Lett.* **90**, 263901 (2007).
14. E. B. Steager, M. S. Sakar, D. H. Kim, V. Kumar, G. J. Pappas, M. J. Kim, Electrokinetic and optical control of bacterial microrobots. *J. Micromech. Microeng.* **21**, 035001 (2011).
15. S. Martel, C. C. Tremblay, S. Ngakeng, G. Langlois, Controlled manipulation and actuation of micro-objects with magnetotactic bacteria. *Appl. Phys. Lett.* **89**, 8–11 (2006).
16. C. K. Schmidt, M. Medina-Sánchez, R. J. Edmondson, O. G. Schmidt, Engineering microrobots for targeted cancer therapies from a medical perspective. *Nat. Commun.* **11**, 1–18 (2020).
17. A. Farzin, S. A. Etesami, J. Quint, A. Memic, A. Tamayol, Magnetic nanoparticles in cancer therapy and diagnosis. *Adv. Healthc. Mater.* **9**, 1901058 (2020).
18. R. W. Carlsen, M. R. Edwards, J. Zhuang, C. Pacoret, M. Sitti, Magnetic steering control of multi-cellular bio-hybrid microswimmers. *Lab Chip* **14**, 3850–3859 (2014).
19. H. Chen, Y. Li, Y. Wang, P. Ning, Y. Shen, X. Wei, Q. Feng, Y. Liu, Z. Li, C. Xu, S. Huang, C. Deng, P. Wang, Y. Cheng, An engineered bacteria-hybrid microrobot with the magnetothermal bioswitch for remotely collective perception and imaging-guided cancer treatment. *ACS Nano* **16**, 6118–6133 (2022).
20. M. B. Akolpoglu, Y. Alapan, N. O. Dogan, S. F. Baltaci, O. Yasa, G. A. Tural, M. Sitti, Magnetically steerable bacterial microrobots moving in 3D biological matrices for stimuli-responsive cargo delivery. *Sci. Adv.* **8**, eabo6163 (2022).
21. O. Felfoul, M. Mohammadi, S. Taherkhani, D. de Lanauze, Y. Zhong Xu, D. Loghin, S. Essa, S. Jancik, D. Houle, M. Lafleur, L. Gaboury, M. Tabrizian, N. Kaou, M. Atkin, T. Vuong, G. Batist, N. Beauchemin, D. Radzioch, S. Martel, Magneto-aerotactic bacteria deliver drug-containing nanoliposomes to tumour hypoxic regions. *Nat. Nanotechnol.* **11**, 941–947 (2016).
22. J. Xing, T. Yin, S. Li, T. Xu, A. Ma, Z. Chen, Y. Luo, Z. Lai, Y. Lv, H. Pan, R. Liang, X. Wu, M. Zheng, L. Cai, Sequential magneto-actuated and optics-triggered biomicrorobots for targeted cancer therapy. *Adv. Funct. Mater.* **31**, 2008262 (2021).
23. B. Shapiro, S. Kulkarni, A. Nacev, S. Muro, P. Y. Stepanov, I. N. Weinberg, Open challenges in magnetic drug targeting. *Wiley Interdiscip. Rev. Nanomed. Nanobiotechnol.* **7**, 446–457 (2015).
24. S.-I. Takeda, F. Mishima, S. Fujimoto, Y. Izumi, S. Nishijima, Development of magnetically targeted drug delivery system using superconducting magnet. *J. Magn. Magn. Mater.* **311**, 367–371 (2007).
25. N. Mirkhani, M. G. Christiansen, S. Schuerle, Living, self-replicating ferrofluids for fluidic transport. *Adv. Funct. Mater.* **30**, 2003912 (2020).
26. S. Schuerle, A. P. Soleimany, T. Yeh, G. Anand, M. Häberli, H. E. Fleming, N. Mirkhani, F. Qiu, S. Hauert, X. Wang, B. J. Nelson, S. N. Bhatia, Synthetic and living micropropellers for convection-enhanced nanoparticle transport. *Sci. Adv.* **5**, eaav4803 (2019).
27. A. S. Bahaj, P. A. B. James, F. D. Moeschler, An alternative method for the estimation of the magnetic moment of non-spherical magnetotactic bacteria. *IEEE Trans. Magn.* **32**, 5133–5135 (1996).
28. S. Seong, T. H. Park, Swimming characteristics of magnetic bacterium, Magnetospirillum sp. AMB-1, and implications as toxicity measurement. *Biotechnol. Bioeng.* **76**, 11–16 (2001).
29. P. Artursson, K. Palm, K. Luthman, Caco-2 monolayers in experimental and theoretical predictions of drug transport. *Adv. Drug Deliv. Rev.* **46**, 27–43 (2001).
30. N. Cruz, L. Qi, X. Alvarez, R. D. Berg, E. A. Deitch, The Caco-2 cell monolayer system as an in vitro model for studying bacterial-enterocyte interactions and bacterial translocation. *J. Burn Care Rehabil.* **15**, 207–212 (1994).
31. M. Yasuda, S. Nagata, S. Yamane, C. Kunikata, Y. Kida, K. Kuwano, C. Suezawa, J. Okuda, *Pseudomonas aeruginosa serA* gene is required for bacterial translocation through Caco-2 cell monolayers. *PLOS ONE* **12**, e0169367 (2017).
32. Z. W. Tay, P. Chandrasekharan, A. Chiu-Lam, D. W. Hensley, R. Dhavalikar, X. Y. Zhou, E. Y. Yu, P. W. Goodwill, B. Zheng, C. Rinaldi, S. M. Conolly, Magnetic particle imaging-guided heating in vivo using gradient fields for arbitrary localization of magnetic hyperthermia therapy. *ACS Nano* **12**, 3699–3713 (2018).
33. J. F. Liu, N. Neel, P. Dang, M. Lamb, J. McKenna, L. Rodgers, B. Litt, Z. Cheng, A. Tsourkas, D. Issadore, J. F. Liu, N. Neel, P. Dang, M. Lamb, J. McKenna, L. Rodgers, B. Litt, Z. Cheng, A. Tsourkas, D. Issadore, Radiofrequency-triggered drug release from nanoliposomes with millimeter-scale resolution using a superimposed static gating field. *Small* **14**, 1802563 (2018).
34. X. Cao, E. Moeendarbary, P. Isermann, P. M. Davidson, X. Wang, M. B. Chen, A. K. Burkart, J. Lammerding, R. D. Kamm, V. B. Shenoy, A chemomechanical model for nuclear morphology and stresses during cell transendothelial migration. *Biophys. J.* **111**, 1541–1552 (2016).
35. S. M. A. Arefi, D. Tsvirkun, C. Verdier, J. J. Feng, A biomechanical model for the transendothelial migration of cancer cells. *Phys. Biol.* **17**, 036004 (2020).
36. P. Panorchan, J. P. George, D. Wirtz, Probing intercellular interactions between vascular endothelial cadherin pairs at single-molecule resolution and in living cells. *J. Mol. Biol.* **358**, 665–674 (2006).
37. J. Escribano, M. B. Chen, E. Moeendarbary, X. Cao, V. Shenoy, J. M. Garcia-Aznar, R. D. Kamm, F. Spill, Balance of mechanical forces drives endothelial gap formation and may facilitate cancer and immune-cell extravasation. *PLOS Comput. Biol.* **15**, e1006395 (2019).
38. R. Szulcek, C. M. L. Beckers, J. Hodzic, J. DeWit, Z. Chen, T. Grob, R. J. P. Musters, R. D. Minshall, V. W. M. Van Hinsbergh, G. P. Van Nieuw Amerongen, Localized RhoA GTPase activity regulates dynamics of endothelial monolayer integrity. *Cardiovasc. Res.* **99**, 471–482 (2013).
39. G. Kornev, Y. Gu, P. Aprelev, A. Tokarev, *Magnetic Characterization Techniques for Nanomaterials* (Springer, 2017), 51–83.

40. R. M. Erb, J. J. Martin, R. Soheilian, C. Pan, J. R. Barber, Actuating Soft Matter with Magnetic Torque. *Adv. Funct. Mater* **26**, 3859–3880 (2016).
41. W. Huang, F. Yang, L. Zhu, R. Qiao, Y. Zhao, Manipulation of magnetic nanorod clusters in liquid by non-uniform alternating magnetic fields. *Soft Matter* **13**, 3750–3759 (2017).
42. F. Hirschhaeuser, H. Menne, C. Dittfeld, J. West, W. Mueller-Klieser, L. A. Kunz-Schughart, Multicellular tumor spheroids: An underestimated tool is catching up again. *J. Biotechnol.* **148**, 3–15 (2010).
43. A. I. Minchinton, I. F. Tannock, Drug penetration in solid tumours. *Nat. Rev. Cancer* **6**, 583–592 (2006).
44. S. B. Suh, A. Jo, M. A. Traore, Y. Zhan, S. L. Coutermarsh-Ott, V. M. Ringel-Scaia, I. C. Allen, R. M. Davis, B. Behkam, Nanoscale bacteria-enabled autonomous drug delivery system (NanoBEADS) enhances intratumoral transport of nanomedicine. *Adv. Sci.* **6**, 1801309 (2019).
45. S. W. Byers, C. L. Sommers, B. Hoxter, A. M. Mercurio, A. Tozeren, Role of E-cadherin in the response of tumor cell aggregates to lymphatic, venous and arterial flow: Measurement of cell-cell adhesion strength. *J. Cell Sci.* **108** (Pt 5), 2053–2064 (1995).
46. D. S. Richardson, J. W. Lichtman, Clarifying tissue clearing. *Cell* **162**, 246–257 (2015).
47. C. T. Lefèvre, M. Bennet, L. Landau, P. Vach, D. Pignol, D. A. Bazylinski, R. B. Frankel, S. Klumpp, D. Faivre, Diversity of magneto-aerotactic behaviors and oxygen sensing mechanisms in cultured magnetotactic bacteria. *Biophys. J.* **107**, 527–538 (2014).
48. S. Riffle, R. S. Hegde, Modeling tumor cell adaptations to hypoxia in multicellular tumor spheroids. *J. Exp. Clin. Cancer Res.* **36**, 102 (2017).
49. N. Mirkhani, T. Gwisai, S. Schuerle, Engineering cell-based systems for smart cancer therapy. *Adv. Intell. Syst.* **4**, 2100134 (2021).
50. M. R. Benoit, D. Mayer, Y. Barak, I. Y. Chen, W. Hu, Z. Cheng, S. X. Wang, D. M. Spielman, S. S. Gambhir, A. Matin, Visualizing implanted tumors in mice with magnetic resonance imaging using magnetotactic bacteria. *Clin. Cancer Res.* **15**, 5170–5177 (2009).
51. A. E. David, A. J. Cole, B. Chertok, Y. S. Park, V. C. Yang, A combined theoretical and in vitro modeling approach for predicting the magnetic capture and retention of magnetic nanoparticles in vivo. *J. Control. Release* **152**, 67–75 (2011).
52. A. K. A. Silva, N. Luciani, F. Gazeau, K. Aubertin, S. Bonneau, C. Chauvierre, D. Letourneur, C. Wilhelm, Combining magnetic nanoparticles with cell derived microvesicles for drug loading and targeting. *Nanomed. Nanotechnol. Biol. Med.* **11**, 645–655 (2015).
53. B. Polyak, I. Fishbein, M. Chorny, I. Alferiev, D. Williams, B. Yellen, G. Friedman, R. J. Levy, High field gradient targeting of magnetic nanoparticle-loaded endothelial cells to the surfaces of steel stents. *Proc. Natl. Acad. Sci. U.S.A.* **105**, 698–703 (2008).
54. B. Gleich, J. Weizenecker, Tomographic imaging using the nonlinear response of magnetic particles. *Nature* **435**, 1214–1217 (2005).
55. M. Graeser, F. Thieben, P. Szwargulski, F. Werner, N. Gdaniec, M. Boberg, F. Griese, M. Möddel, P. Ludewig, D. van de Ven, O. M. Weber, O. Woywode, B. Gleich, T. Knopp, Human-sized magnetic particle imaging for brain applications. *Nat. Commun.* **10**, 1–9 (2019).
56. Y. Qiu, S. Tong, L. Zhang, Y. Sakurai, D. R. Myers, L. Hong, W. A. Lam, G. Bao, Magnetic forces enable controlled drug delivery by disrupting endothelial cell-cell junctions. *Nat. Commun.* **8**, 1–10 (2017).
57. G. R. Kale, X. Yang, J. M. Philippe, M. Mani, P. F. Lenne, T. Lecuit, Distinct contributions of tensile and shear stress on E-cadherin levels during morphogenesis. *Nat. Commun.* **9**, 1–16 (2018).
58. M. Aubry, W. A. Wang, Y. Guyodo, E. Delacou, J. M. Guigner, O. Espeli, A. Lebreton, F. Guyot, Z. Gueroui, Engineering *E. coli* for magnetic control and the spatial localization of functions. *ACS Synth. Biol.* **9**, 3030–3041 (2020).
59. C. R. Grant, M. Amor, H. A. Trujillo, S. Krishnapura, A. T. Iavarone, A. Komeili, Distinct gene clusters drive formation of ferrosome organelles in bacteria. *Nature* **606**, 1–5 (2022).
60. S. Taherkhani, M. Mohammadi, J. Daoud, S. Martel, M. Tabrizian, Covalent binding of nanoliposomes to the surface of magnetotactic bacteria for the synthesis of self-propelled therapeutic agents. *ACS Nano* **8**, 5049–5060 (2014).
61. H. C. Berg, *Random Walks in Biology: New and Expanded Edition* (Princeton University Press, 1993).
62. Y. Yang, Y. Zhao, Discretized motion of surface walker under a nonuniform ac magnetic field. *Langmuir* **36**, 11125–11137 (2020).
63. J. Fan, Z. Sun, J. Zhang, Q. Huang, S. Yao, Y. Zong, Y. Kohmura, T. Ishikawa, H. Liu, H. Jiang, Quantitative imaging of single unstained magnetotactic bacteria by coherent x-ray diffraction microscopy. *Anal. Chem.* **87**, 5849–5853 (2015).
64. Y. Gongyang, W. Ouyang, C. Qu, M. Urbakh, B. Quan, M. Ma, Q. Zheng, Temperature and velocity dependent friction of a microscale graphite-DLC heterostructure. *Friction* **8**, 462–470 (2020).
65. T. J. Silhavy, D. Kahne, S. Walker, The bacterial cell envelope. *Cold Spring Harb. Perspect. Biol.* **2**, a000414 (2010).
66. K. Dutta, D. Hu, B. Zhao, A. E. Ribbe, J. Zhuang, S. Thayumanavan, Templated self-assembly of a covalent polymer network for intracellular protein delivery and traceless release. *J. Am. Chem. Soc.* **139**, 5676–5679 (2017).
67. Y. Anraku, A. Kishimura, M. Kamiya, S. Tanaka, T. Nomoto, K. Toh, Y. Matsumoto, S. Fukushima, D. Sueyoshi, M. R. Kano, Y. Urano, N. Nishiyama, K. Kataoka, Systemically injectable enzyme-loaded polyion complex vesicles as in vivo nanoreactors functioning in tumors. *Angew. Chem. Int. Ed.* **55**, 560–565 (2016).

Acknowledgments: We thank the EPIC RCHCI staff and management and the ETHZ animal welfare officers for their great support with animal experiments. We also thank the Scientific Center for Optical and Electron Microscopy (ScopeM) and the Flow Cytometry Core Facility at ETH-Zürich for access to facilities. We thank D. C. Bono for useful input for the magnetometer design, L. Amoudruz for helpful discussions on computational modeling of MTB, L. Stöcklin for assistance with the inductive detection experiments, and D. Dubey for providing helpful feedback on the manuscript. **Funding:** This work is supported by the Branco Weiss Fellowship—Society in Science (title: "Cancer-fighting magnetic biobots: Harnessing the power of synthetic biology and magnetism") and funding from Takeda Pharmaceuticals (title: "Feasibility study: Penetration ability of magnetotactic bacteria"). T.G. was supported by a Swiss Government Excellence Scholarship. **Author contributions:** Conceptualization: S.S., T.G., N.M., M.G.C., and V.L. Methodology: S.S., T.G., N.M., and M.G.C. Investigation: T.G., N.M., M.G.C., T.T.N., and S.S. Visualization: T.G. Supervision: S.S. Writing—original draft: T.G. Writing—review and editing: S.S., T.G., M.G.C., N.M., T.T.N., and V.L. **Competing interests:** S.S. is co-founder, technical advisor, and member of the board of MagnebotiX AG and member of the board of Quercis Pharma. AG. V.L. is an employee of Takeda Pharmaceuticals. The authors declare that they have no other competing interests. **Data and materials availability:** All data needed to support the conclusions of this manuscript are included in the main text or Supplementary Materials. Additional data related to this paper may be requested from the authors.

Submitted 11 January 2022
Accepted 3 October 2022
Published 26 October 2022
10.1126/scirobotics.abo0665

Science Robotics

Magnetic torque–driven living microrobots for increased tumor infiltration

T. Gwisai, N. Mirkhani, M. G. Christiansen, T. T. Nguyen, V. Ling, and S. Schuerle

Sci. Robot. **7** (71), eabo0665. DOI: 10.1126/scirobotics.abo0665

Science Robotics (ISSN 2470-9476) is published by the American Association for the Advancement of Science. 1200 New York Avenue NW, Washington, DC 20005. The title *Science Robotics* is a registered trademark of AAAS.